Supporting Information

Carbon layer confined Co-Ni bimetallic oxide heterojunctions for high-efficiency electrosynthesis of 2,5-furandicarboxylic acid

Zhong Cheng,[a,c] Jing Hu,[a] Wenjing Zhou,[a] Wenfang Deng,[a,b,*] Ming Ma,[a,*] and Yueming Tan,[a,*]

[a] Key Laboratory of Chemical Biology and Traditional Chinese Medicine Research (Ministry of Education of China), College of Chemistry and Chemical Engineering, Hunan Normal University, Changsha 410081, China

[b] Institute of Interdisciplinary Studies, Hunan Normal University, Changsha 410081, China

[c] College of Chemistry and Chemical Engineering, Hunan University, Changsha, Hunan 410082, China

E-mail: Dengwenfang@hunnu.edu.cn (W. Deng); mingma@hunnu.edu.cn (M. Ma); tanyueming0813@hunnu.edu.cn (Y. Tan).

Chemicals. The chemicals of D-glucose (AR), Cobalt acetate tetrahydrate ($Co(acac)_2 \cdot 4H_2O$, AR), Nickel acetate tetrahydrate ($Ni(acac)_2 \cdot 4H_2O$, AR) and anhydrous ethanol (AR) were purchased from Sinopharm Chemical Reagent Co. Ltd. The chemicals of 5-hydroxymethylfurfural (HMF), 2,5-furandicarboxylic acid (FDCA), 5-hydroxymethyl-2-furancarboxylic acid (HMFCA), 2,5-diformylfuran (DFF), 5-formyl-2-furancarboxylic acid (FFCA), Nafion (5 wt%) were purchased from Sigma-Aldric. Nickel foam (NF) was purchased from Sheng Qiang Co. Ltd. Deionized (DI) water (18.25 $M\Omega\ cm^{-1}$) from a system (Milli-Q) was used in all experiments. All the chemicals were used without purification.

Instrumentation. Scanning electron microscope (SEM) images were taken by a FEI SEM450. Scanning transmission electron micrographs (STEM), HAADF-STEM images and energy dispersive X-ray spectroscopy (EDS) elemental mapping were carried out on a Thermo Fisher Scientific Talos F200X S/TEM instrument with an accelerating voltage of 200 kV, respectively. X-ray diffraction (XRD) patterns were obtained with an Ultima IV powder diffractometer using Cu Kα radiation (λ = 1.5406 Å). X-ray photoelectron spectra (XPS) was detected by the Thermo ESCALAB 250Xi (Thermo Electron, U.K.) with Al Kα X-ray source. The Raman spectra were recorded at room temperature on a Thermo DXR instrument with a 780 nm excitation laser. N_2 adsorption-desorption test was carried out at 77 K using a Micromeritics ASAP 2460 instrument. Zeta potential was performed by Britain-Malvern-Zetasizer Nano ZS90 potential analyzer device. In situ Raman spectra were characterized by the confocal Raman microscope (Horiba JY HR Evolution with 532 nm laser). All electrochemical experiments were performed on a CHI760E electrochemical workstation. The catalyst ink modified nickel foam was used as the working electrode, and a Pt foil (1 cm^2) and a HgO/Hg (1.0 M KOH) electrode served as the counter and reference electrodes, respectively.

HPLC analysis. HPLC (Shimadzu Prominence LC-20AT, Japan), which detector is an ultraviolet-visible detector, was used to analyze HMF and corresponding selective oxidation products. In general, 50 μL of electrolyte was obtained during potentiostatic electrolysis and diluted to 2 ml with ultrapure water, filtrated and analyzing it by HPLC. The wavelength of the UV detector is set to 265 nm, mobile phase A was 5 mM ammonium formate aqueous solution and phase B was methanol, the ratio of A:B is 7:3, flow rate is 0.6 mL min^{-1}. Using a 4.6 mm × 250 mm Spherigel GWS 5 μm C18 column, each separation lasts for 12 minutes.

The theoretic total charge of HMF electrooxidation is as follows:

$$6 \times (20\ mL) \times (10\ mM) \times (6.02 \times 10^{23}\ mol/L) \times (1.6 \times 10^{-19}\ C) = 116\ C$$

The HMF conversion (%), FDCA yield (%) and faradaic efficiency (%) were calculated using equations (1), (2) and (3), respectively.

$$\text{HMF conversion} = (\text{mol of HMF consumed}) / (\text{mol of initial HMF}) \times 100 \quad (1)$$

$$\text{FDCA yield} = (\text{mol of FDCA formed}) / (\text{mol of initial HMF}) \times 100 \quad (2)$$

$$\text{Faradaic efficiency} = (6 \times F) \times (\text{mol of FDCA formed}) / (\text{total charge}) \times 100 \quad (3)$$

Theoretical calculation. All density functional theory (DFT) calculations were conducted via the Vienna ab initio simulation package (VASP). The generalized gradient approximation (GGA) functional of Perdew, Burke, and Ernzerhof (PBE) was employed for the electron exchange and correlation energy for structural relaxation. The energy cutoff for the plane wave basis expansion was set to 450 eV and the force on each atom less than 0.02 eV/Å was set for the convergence criterion of geometry relaxation. The energy convergence criterion was 10^{-4} eV. A vacuum layer of 20 Å was adopted to avoid the interaction between contiguous period layers. The Ni(200) and Co_3O_4(220) surfaces were chosen to construct the

heterojunction structure taking into account the crystal plane and lattice matching rules. The HMF adsorption energy was calculated by the following equation:

$$E_{\text{surface-HMF}} = E_{\text{surface-HMF}} - E_{\text{surface}} - E_{\text{HMF}}$$

where $E_{\text{surface-HMF}}$, E_{surface} and E_{HMF} represent the total energy of the pristine surface with HMF, surface energies and the energy of HMF, respectively. The Gibbs free energy change (ΔG) of each step is calculated using the following formula:

$$\Delta G = \Delta E + \Delta ZPE - T\Delta S$$

where ΔE is the electronic energy difference directly obtained from DFT calculations, ΔZPE is the zero point energy difference, T is the room temperature (298.15 K) and ΔS is the entropy change. ZPE could be obtained after frequency calculation.

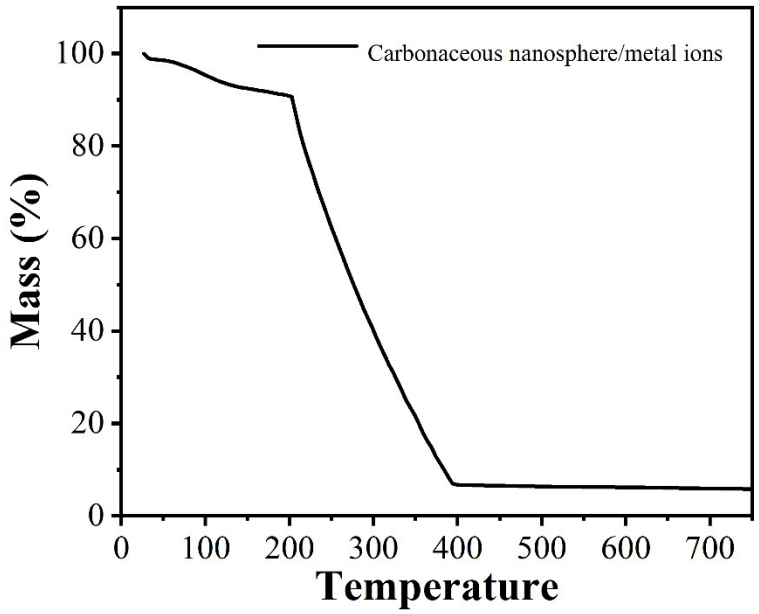

Fig. S1. TGA profile of CNS/metal ions in an air atmosphere.

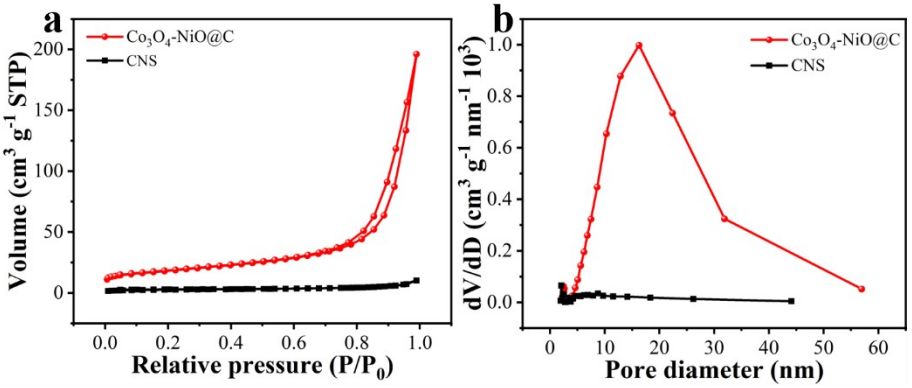

Fig. S2. (a) N_2 adsorption–desorption isotherms and (b) pore size distribution of Co_3O_4-NiO@C and CNS.

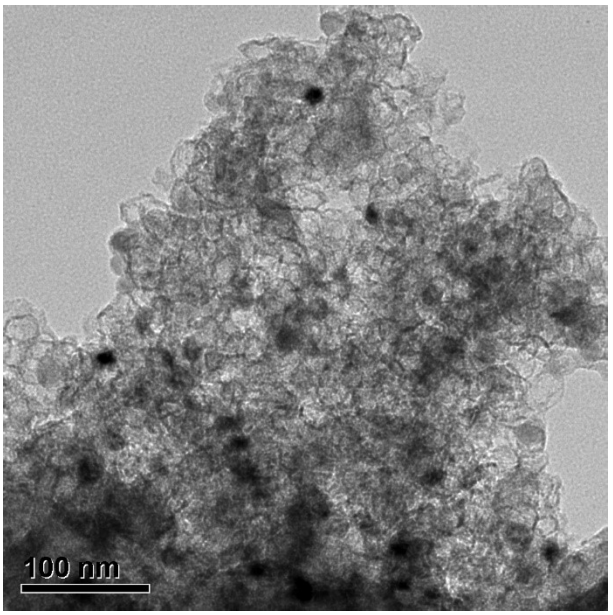

Fig. S3. TEM image of Co_3O_4-NiO@C after acid treatment.

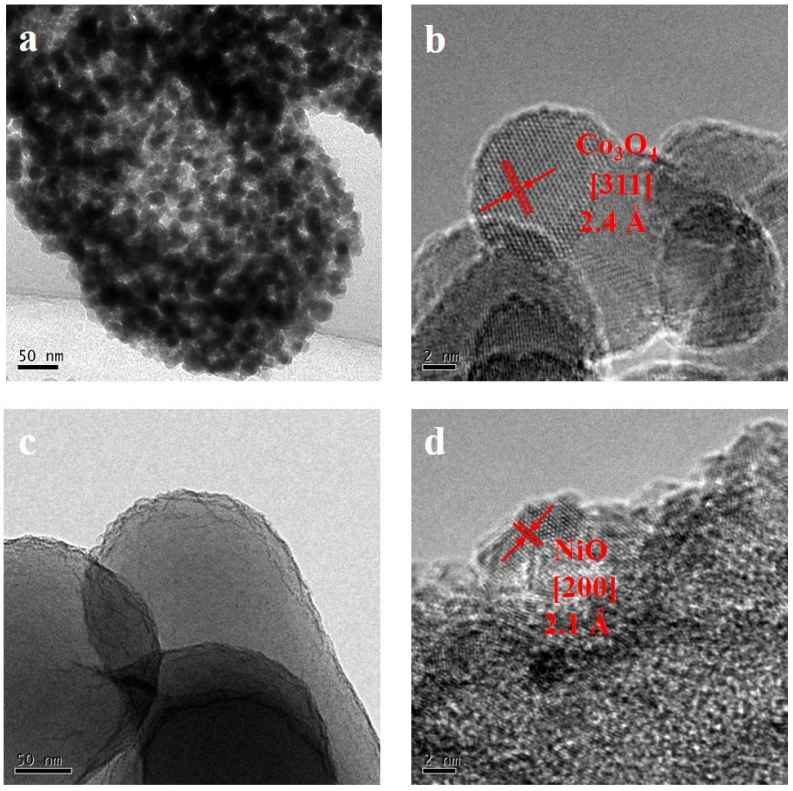

Fig. S4. TEM and HRTEM images of (a, b) Co_3O_4@C and (c, d) NiO@C.

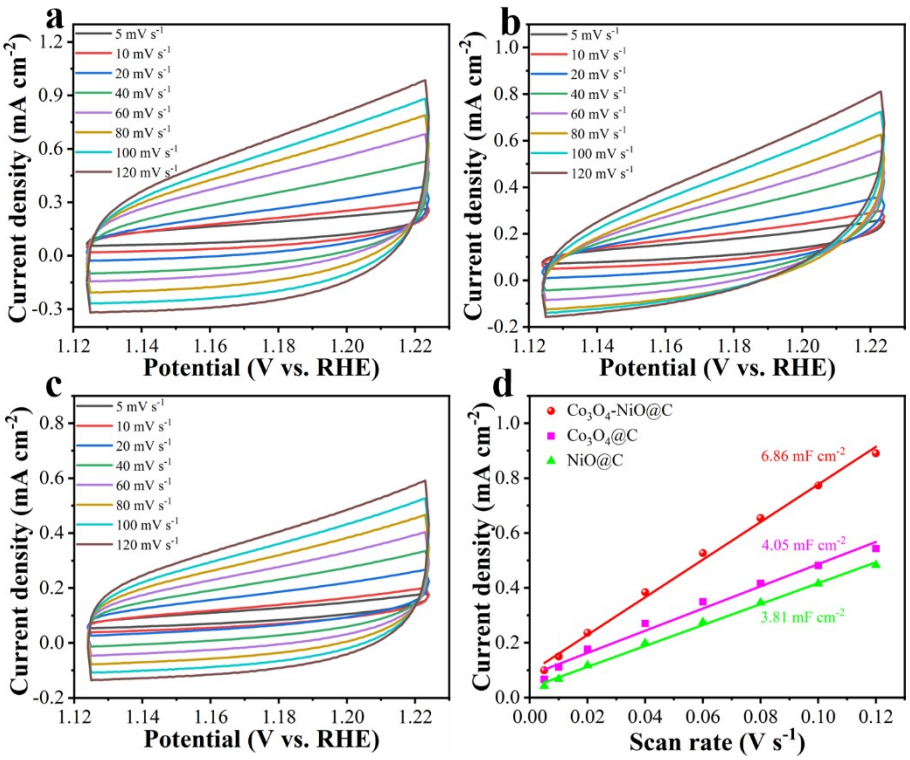

Fig. S5. CVs curves of (a) Co_3O_4-NiO@C, (b) Co_3O_4@C, and (c) NiO@C at various scan rates (5 to 120 mV s^{-1}), respectively. (d) Corresponding C_{dl} of Co_3O_4-NiO@C, Co_3O_4@C, and NiO@C.

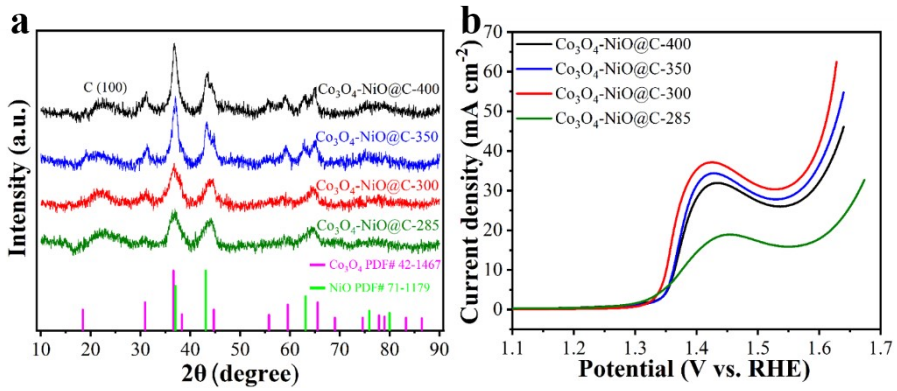

Fig. S6. (a) XRD patterns of Co_3O_4-NiO@C prepared at different calcination temperatures. (b) LSV curves of Co_3O_4-NiO@C prepared at different calcination temperatures in 1 M aqueous KOH containing 50 mM HMF.

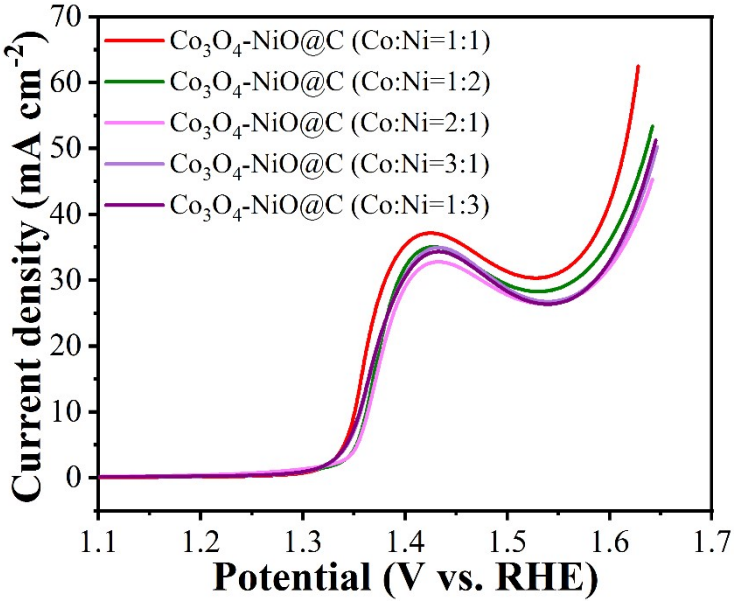

Fig. S7. LSV curves of Co_3O_4-NiO@C prepared at different Co/Ni ratios in the precursors in 1 M KOH + 50 mM HMF aqueous solution.

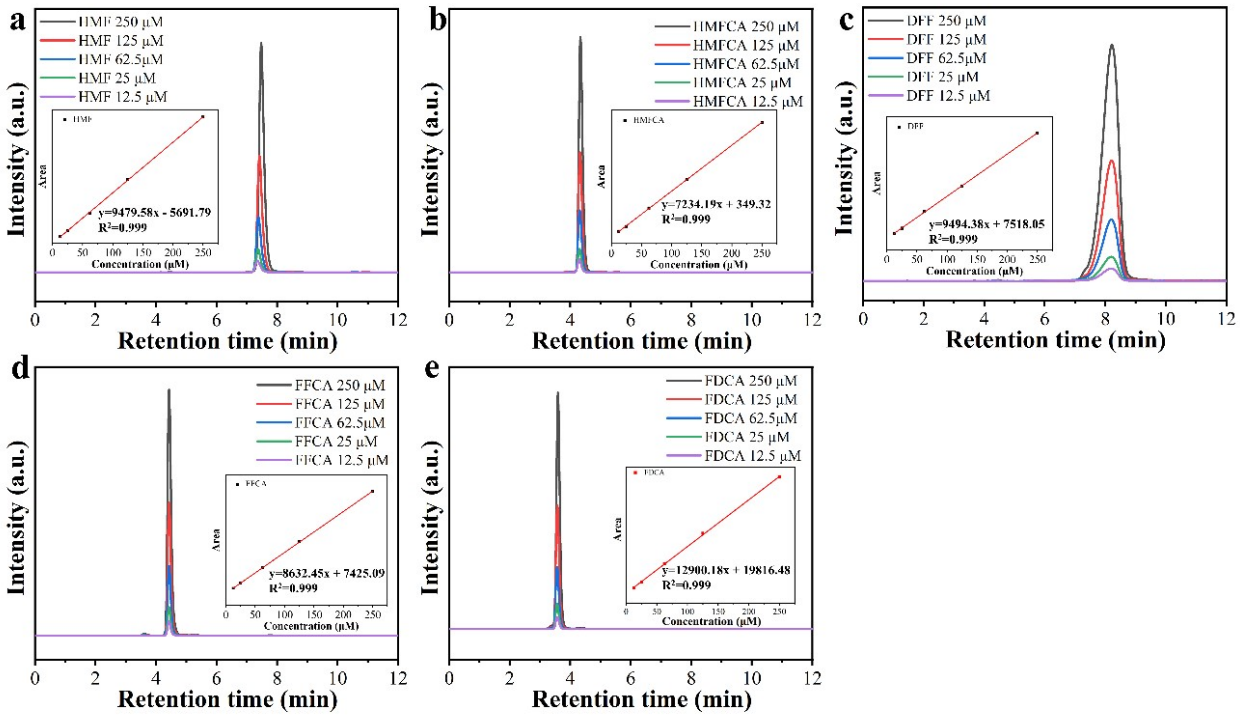

Fig. S8. The HPLC standard curves of (a) HMF, (b) HMFCA, (c) DFF, (d) FFCA, and (e) FDCA.

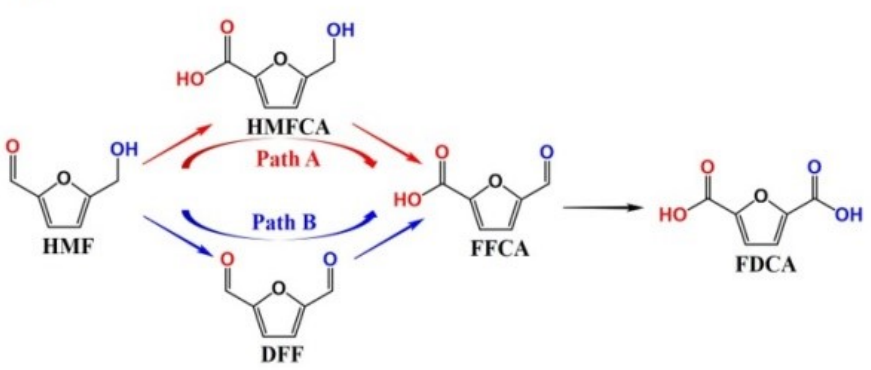

Fig. S9. Two possible pathways of HMF oxidation to FDCA.

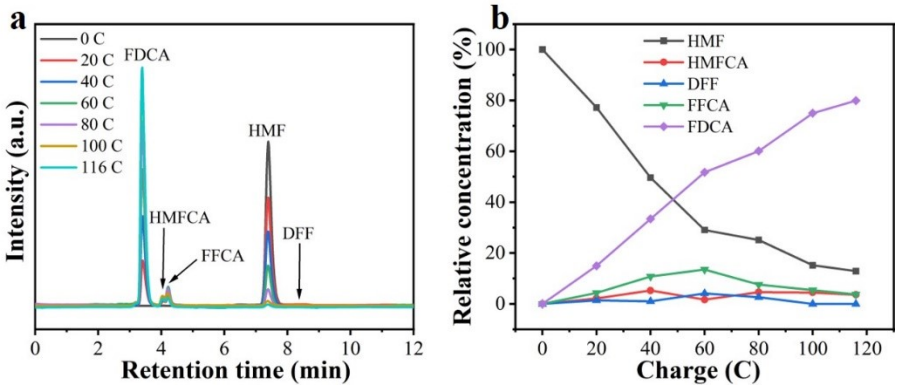

Fig. S10. (a) HPLC elution profiles and (b) conversion changes of HMF electrooxidation catalyzed by Co_3O_4@C with the increasing of charge.

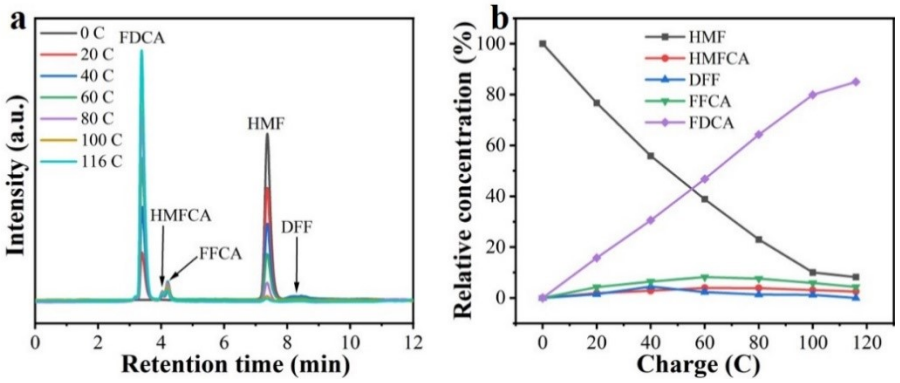

Fig. S11. (a) HPLC elution profiles and (b) conversion changes of HMF electrooxidation catalyzed by NiO@C with the increasing of charge.

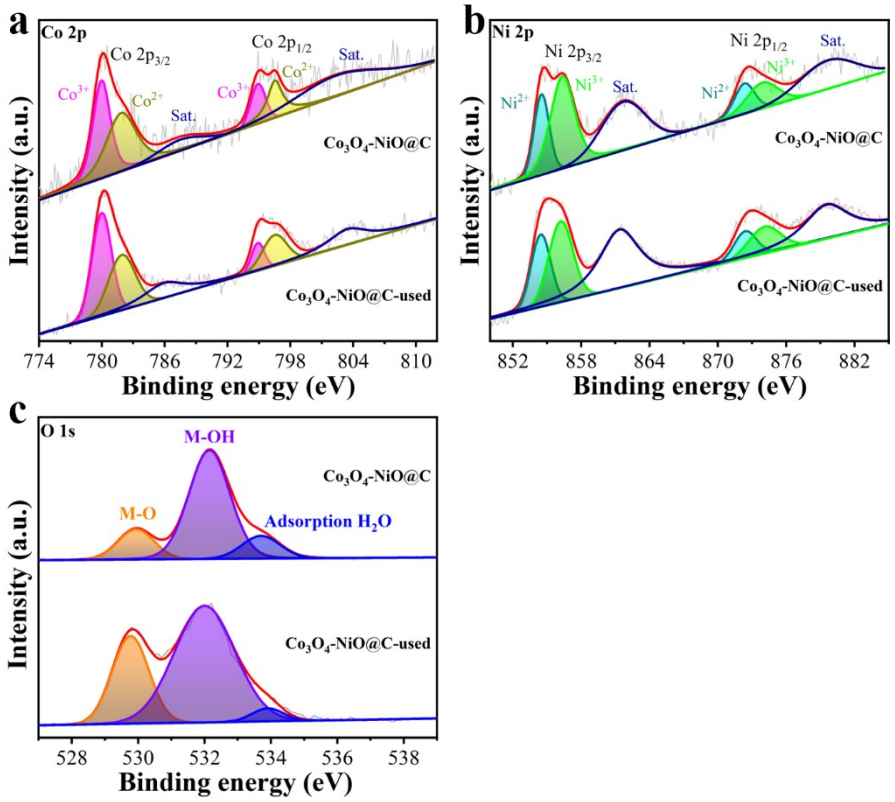

Fig. S12. Corresponding high-resolution XPS spectrum of Co_3O_4-NiO@C and Co_3O_4-NiO@C-used for (a) Co 2p, (b) Ni 2p and (c) O 1s.

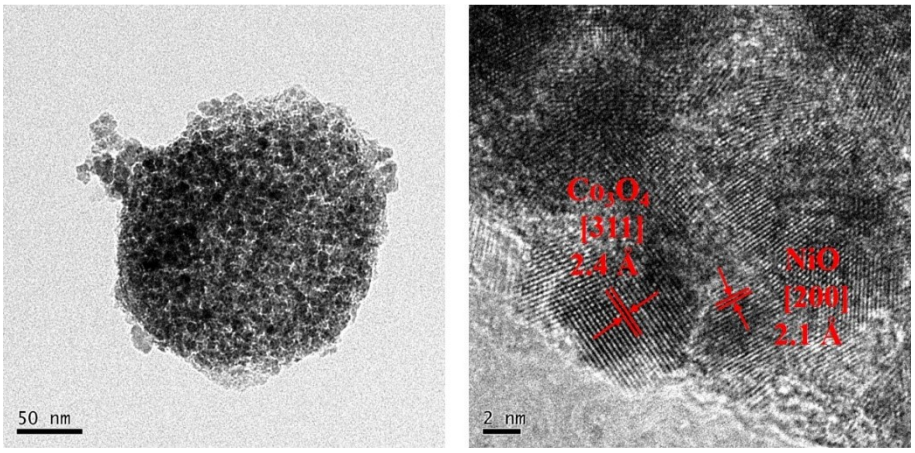

Fig. S13. (a) TEM and (b) HRTEM images of the Co_3O_4-NiO@C after HMFOR.

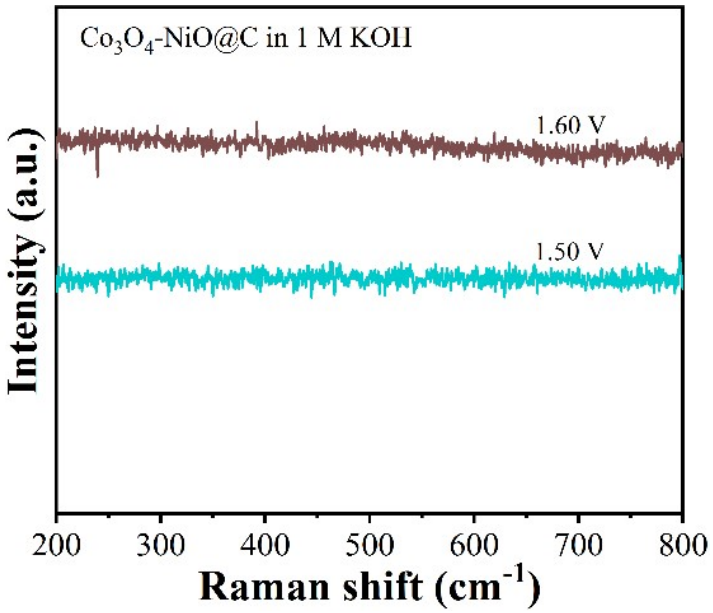

Fig. S14. In situ Raman spectra of Co_3O_4-NiO@C in 1 M aqueous KOH at 1.5 and 1.6 V.

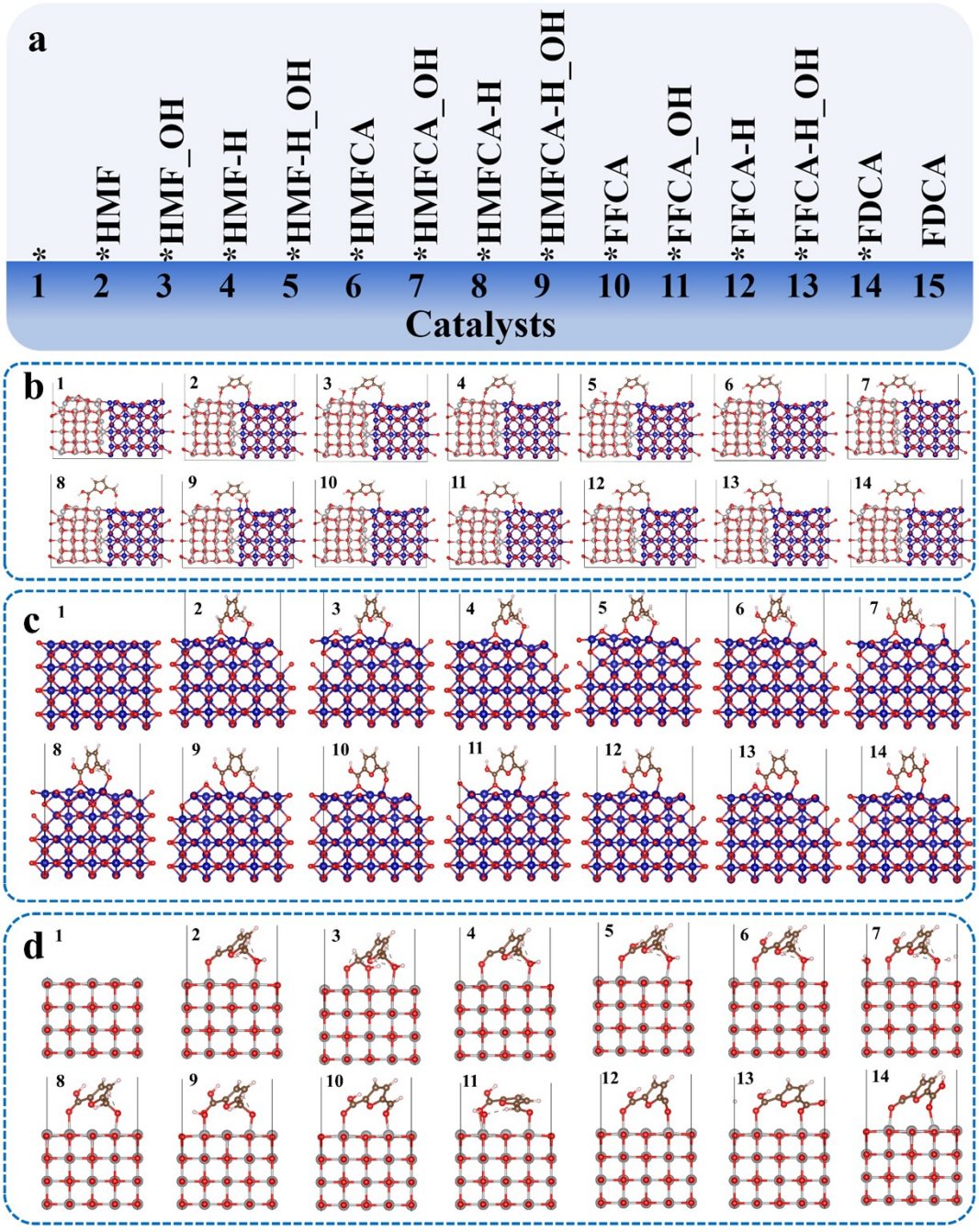

Fig. S15. (a) The reaction pathway for HMFOR on the catalysts. Theoretical computational models of the reaction pathway for HMFOR on (b) Co_3O_4-NiO@C, (c) Co_3O_4 and (d) NiO.

Table S1. Comparison of HMFOR performance for Co_3O_4-NiO@C and other reported catalysts.

Electrocatalyst	Oxidation Potential (V)	HMF Conversion (%)	FDCA yield (%)	FE (%)	Ref.
Ni_2P NPA/NF	1.423	99.9	99.9	99.7	[1]
Ni_3S_2/NF	1.423	>99	98	98	[2]
Ni_3N@C	1.4	>99	98	~99	[3]
MoO_2-FeP@C	1.424	99.4	98.6	98.7	[4]
NiCoP	1.464	99.9	98.9	94.2	[5]
$CuCo_2O_4$	1.45	98	93.7	94	[6]
NiSe@NiO_x	1.423	99	98	98	[7]
Ir-Co_3O_4	1.42	>99	98	98	[8]
$NiCo_2O_4$@NF	1.5	99.6	90.8	87.5	[9]
CoFe@NiFe	1.5	>99	97	NA	[10]
Pt/$Ni(OH)_2$	NA	>99	98.7	~100	[11]
InOOH-O_V	1.48	98.5	91.6	~91.5	[12]
Co_3O_4-NiO@C	1.4	99.1	99.1	98.9	This work

Table S2. NiO and Co_3O_4 heterogeneous crystal matching.

	NiO(200)	Co_3O_4(220)	Heterojunction	Mis-match (NiO)	Mis-match (Co_3O_4)
a	8.295	8.046	8.209	-0.76%	+1.8%
b	12.442	11.379	11.911	-4.27%	+4.68%
α	90	90	90	0	0
β	90	90	90	0	0
γ	90	90	90	0	0

References

1. B. You, N. Jiang, X. Liu and Y. Sun, *Angew. Chem. Int. Ed.*, 2016, **55**, 9913-9917.
2. B. You, X. Liu, N. Jiang and Y. Sun, *J. Am. Chem. Soc.*, 2016, **138**, 13639-13646.
3. N. Zhang, Y. Zou, L. Tao, W. Chen, L. Zhou, Z. Liu, B. Zhou, G. Huang, H. Lin and S. Wang, *Angew. Chem. Int. Ed.*, 2019, **131**, 16042-16050.
4. G. Yang, Y. Jiao, H. Yan, Y. Xie, A. Wu, X. Dong, D. Guo, C. Tian and H. Fu, *Adv. Mater.*, 2020, **32**, 2000455-2000464.
5. H. Wang, C. Li, J. An, Y. Zhuang and S. Tao, *J. Mater. Chem. A*, 2021, **9**, 18421-18430.
6. Y. Lu, C. L. Dong, Y. C. Huang, Y. Zou, Z. Liu, Y. Liu, Y. Li, N. He, J. Shi and S. Wang, *Angew. Chem. Int. Ed.*, 2020, **59**, 19215-19221.
7. L. Gao, Z. Liu, J. Ma, L. Zhong, Z. Song, J. Xu, S. Gan, D. Han and L. Niu, *Appl. Catal. B-Environ.* , 2020, **261**, 118235.
8. Y. Lu, T. Liu, C. L. Dong, Y. C. Huang, Y. Li, J. Chen, Y. Zou and S. Wang, *Adv. Mater.*, 2021, **33**, 2007056.
9. M. J. Kang, H. Park, J. Jegal, S. Y. Hwang, Y. S. Kang and H. G. Cha, *Appl. Catal. B-Environ.* , 2018, **242**, 85-91.
10. Y. Xie, Z. Zhou, N. Yang and G. Zhao, *Adv. Funct. Mater.*, 2021, **31**, 2102886.
11. B. Zhou, Y. Li, Y. Zou, W. Chen, W. Zhou, M. Song, Y. Wu, Y. Lu, J. Liu, Y. Wang and S. Wang, *Angew. Chem. Int. Ed.*, 2021, **60**, 22908-22914.
12. F. Ye, S. Zhang, Q. Cheng, Y. Long, D. Liu, R. Paul, Y. Fang, Y. Su, L. Qu, L. Dai and C. Hu, *Nat. Commun.*, 2023, **14**, 2040.